Available online at www.sciencedirect.com
SCIENCE DIRECT
ELSEVIER
European Journal of Mechanics B/Fluids 25 (2006) 137–152
EUROPEAN JOURNAL OF MECHANICS B/FLUIDS

Separation control at hydrofoils using Lorentz forces

G. Mutschke [a,*], G. Gerbeth [a], T. Albrecht [b], R. Grundmann [b]

[a] *Forschungszentrum Rossendorf, MHD Department, P.O. Box 51 01 19, D-01314 Dresden, Germany*
[b] *Dresden University of Technology, Faculty of Mechanical Engineering, Institute of Aviation and Astronautics Technology, D-01062 Dresden, Germany*

Received 6 September 2004; accepted 6 May 2005

Available online 1 September 2005

Abstract

Lorentz forces originating from surface-mounted actuators of permanent magnets and electrodes in weakly conducting fluids like seawater can be used to control flow separation at hydrofoils. The numerical results presented here are based on direct numerical simulation in the laminar flow regime, limited to Reynolds numbers of O(500). Control by steady forcing at the suction side and by oscillatory forcing near the leading edge of the foil is investigated in the post-stall regime.

By applying a strong enough steady control, separation can be completely suppressed. Oscillatory forcing always has to compete with the natural shedding process, lock-in behavior may occur. Lift-optimum control for strong amplitudes is found in a frequency band around the natural shedding frequency. In terms of the momentum coefficient describing the control effort, appropriate excitation frequencies in relation to the natural vortex shedding frequency allow for a more effective lift control than steady forcing.

Keywords: Electromagnetic flow control; Separation control; Direct numerical simulation

1. Introduction

Separation control is an important issue in many industrial, aviation and marine applications. A large variety of different control methods exists, a general overview of which can be found in [1]. Although intensive studies have been performed to apply steady control schemes, recently it became clear that active control or even just time-periodic control allows for more distinct benefits in many flow configurations. From the literature it is known that applying proper time-periodic blowing and suction can enhance the lift of airfoils considerably in certain flow regimes and is furthermore more efficient than steady blowing, i.e. at the same value of the momentum coefficient, a larger gain in lift can be achieved. For an overview and the basic principles we refer to Greenblatt and Wygnanski [2]. The explanation is based on the excitation of the separating shear-layer, thereby using far-field momentum to advantageously reorganize the vortex shedding process at the suction side. As an example of numerical work, Wu et al. [3] have performed two-dimensional RANS simulations of the turbulent flow over an airfoil at post-stall angles of attack when periodic blowing-suction near the leading edge is applied. In certain ranges of forcing frequencies and angles of attack the unforced random separated flow became periodic or quasi-periodic, associated with significant lift enhancement. The

* Corresponding author. Tel.: +49 351 260 2373; fax: +49 351 260 2007.
E-mail address: G.Mutschke@fz-rossendorf.de (G. Mutschke).

0997-7546/$ – see front matter
doi:10.1016/j.euromechflu.2005.05.002

physical mechanisms responsible for this control are explained to be the non-linear mode competition of the two basic constituents of the flow, the leading-edge shear layer and the vortex shedding from the trailing edge. Optimum control frequencies with respect to lift enhancement typically are of O(1) based on chord length and free stream velocity.

In this paper, we are concerned with applying Lorentz forces into the boundary layer region. These forces are being created by surface setups of electrodes and magnets. What we have in mind are saltwater flows or electrolytes in electrochemical applications where the electric conductivity is typically of the order of 10 S/m. Therefore, induction effects are weak, and, apart from externally applied magnetic fields, electric currents should be fed to the fluid in order to generate Lorentz forces large enough for achieving control.

First efforts in applying Lorentz forces to weakly-conducting fluids were undertaken more than 40 years ago [4,5]. Meanwhile, control of turbulent boundary layers [6–10] and control of the flow around a circular cylinder [11,12] have been discussed extensively. Only recently, first experimental results on the separation control of flow around hydrofoils were published [13,14].

Due to the momentum modification of the near-wall flow, there is a clear similarity to control methods applying suction or blowing in separation control on airfoils which will be outlined in more detail below. As compared to conventional suction/blowing, an advantage of the Lorentz force approach is that the force amplitude is easily adjustable in time by applying alternating currents (up to high frequencies). As compared to steady Lorentz forcing, time-oscillatory forcing may also avoid the side effect of electrolytic bubble generation in seawater.

In the direct numerical simulation presented in this paper, we are limited to relatively low chord Reynolds numbers. Although most potential applications for flow control experience turbulent flow conditions, there is also particular interest in the transitional and low-Reynolds-number range of $Re \sim \mathrm{O}(10^4)$ (e.g. in aviation: RPV's, UAV's etc. [15], active side-hydrofoils for stabilizing cruisers). In numerical simulations, studying the dynamics of large-scale flow structures in a laminar regime allows for an easier understanding of the basic control effects, furthermore excluding any potential uncertainty due to turbulence modeling. This holds especially for oscillatory control which leads to lift enhancements at airfoils or hydrofoils due to a complex coupling of shear layer instability, separation bubble and wake characteristics. We suppose that, although there are essential differences between laminar and turbulent flows, the basic mechanisms of this control approach, as shown by Wu and Wygnanski for the turbulent range [2,3], should also hold in the laminar flow regime. Recently, time-periodic excitation by conventional blowing/suction [16] as well as by applying Lorentz forces [13,14] was proven to achieve control in the transitional range. For laminar flow we expect the near wake including the separation bubble to couple stronger to the shear layer as compared to turbulent flow; this might have an influence on the appropriate control strategy to apply.

First numerical simulations of Hoarau et al. [17] to investigate the 3-D transition around a NACA-0012 airfoil reveal certain similarities in the transition process with the cylinder case, e.g. with respect to least-stable modes and Strouhal frequency if based on the stream-normal length of the foil. Posdziech [11] and Weier et al. [18] have investigated the generic problem of the flow around a circular cylinder under control of a surface-tangential steady Lorentz force. At moderate Reynolds numbers, 2-D tangential forcing is expected to weaken 3-D flow phenomena. Also by Poncet [19] in case of a rotationally oscillating cylinder it was found that 3-D instabilities, occurring at Reynolds numbers larger than 190, become weakened by rotation. This gives reason to us to present 2-D simulations here in a first step.

Furthermore, in rotary or oscillatory control of the cylinder flow, several authors have reported on a lock-in behavior between excitation frequency and vortex shedding frequency [20–22]. Although the coupling influence between actuation frequency, shear layer and the wake structure decreases as the Reynolds number increases, appropriate control techniques can lead to, e.g., considerably reduced drag values as the near wake becomes modified [23,24]. Therefore, also for the flow around an hydrofoil considered here, a large control receptivity at excitation frequencies close to or slightly above the main shedding frequency of the uncontrolled flow should be expected. At larger frequencies, receptivity naturally should decrease because of inertia.

2. Hydrofoil, actuator and governing equations

2.1. Hydrofoil profile

The characteristic polynom of the hydrofoil under investigation is

$$p(x) = d(a_1\sqrt{x} + a_2 x + a_3 x^2 + a_4 x^3 + a_5 x^4) \tag{1}$$

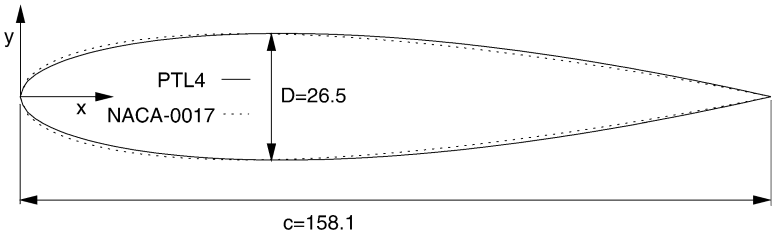

Fig. 1. Comparison of the PTL-4 hydrofoil with the shape of a NACA-0017 profile.

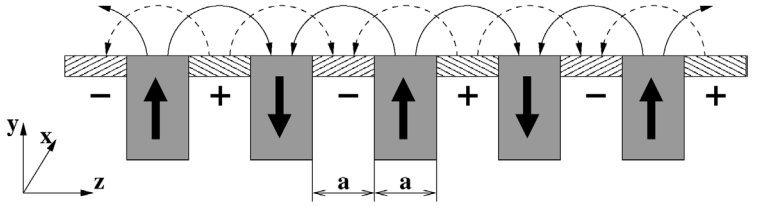

Fig. 2. Sketch (cross-cut) of the actuator for generating a streamwise (x) Lorentz force.

where $0 \leqslant x \leqslant 1$ denotes the streamwise coordinate scaled with the chordlength c. The polynom coefficients are:

$$d = 0.1676154, \qquad a_1 = 1.26854, \tag{2}$$

$$a_2 = 0.292071, \qquad a_3 = -1.34964, \tag{3}$$

$$a_4 = 0.478002, \qquad a_5 = -0.104831. \tag{4}$$

This particular profile was chosen because it later allows for comparison with experimental results. As can be seen from Fig. 1, the profile is very close to the shape of a standard NACA-0017 profile. However, those shape details should only be of minor interest for the first investigations presented here.

2.2. Actuator

The Lorentz force results from the cross product of current density **j** and magnetic induction **B**, whereby the current density is given by Ohm's law in moving media:

$$\mathbf{f}_L = \mathbf{j} \times \mathbf{B}, \quad \mathbf{j} = \sigma(\mathbf{E} + \mathbf{u} \times \mathbf{B}). \tag{5}$$

Because of a relatively low value of the electric conductivity of seawater ($\sigma \approx 10$ S/m), induced currents are in general small for moderate values of the magnetic field strength, and external currents have to be applied in order to achieve any control. In the following we assume that only the externally applied electric field $\mathbf{E}_0$ and magnetic field $\mathbf{B}_0$ contribute to the Lorentz force.[1]

A sketch of the actuator (cross-cut) for generating a streamwise (x) Lorentz force is shown in Fig. 2. It consists of an alternate arrangement of stripes of electrodes of varying polarity and permanent magnets of varying magnetization direction (black arrows). Hereby, the width of both electrodes and permanent magnets is assumed to be equal to a. Surface flush mounted, due to the crossing electric (dashed) and magnetic (solid) field lines, it creates a streamwise (x) volume force in the fluid which is assumed to be electrically conducting (conductivity σ). Assuming hard ferromagnetic properties, the magnetic field of the chain of magnets can easily be calculated analytically. Hereby, the exact result depends on the aspect ratio (y/x) of the magnets. Using a conformal mapping technique, also the current distribution of the electrode array can be found in closed form [11,26]. As a result, apart from inhomogeneities in the

[1] Note that this approach is opposite to general considerations about the energetic efficiency of Lorentz force devices for achieving drag reduction in boundary layers where obviously Ohmic losses should be minimized, i.e. magnetic field strength should be maximum. Then, externally applied currents can be of the same order as those originating from the ($\mathbf{u} \times \mathbf{B}$)-term [25].

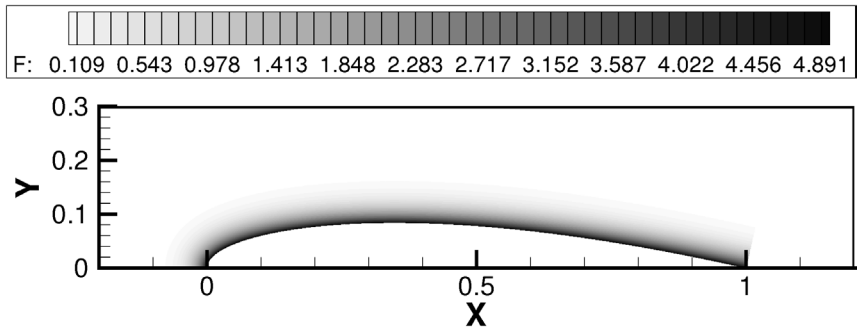

Fig. 3. Spatial force distribution $|\mathbf{f}_L|$ at $a/c = 0.1265$ of amplitude $\frac{\pi}{8} j_0 M_0 = 5$.

near-wall region close to the magnet corners, the Lorentz force pointing in the streamwise x-direction decays exponentially in wall-normal direction. Finally, when averaging over the spanwise direction z, the approximated 2-D form of the Lorentz force density reads

$$\mathbf{f}_L = \sigma \mathbf{E}_0 \times \mathbf{B}_0 = \frac{\pi}{8} j_0 M_0 \, \mathrm{e}^{-(\pi/a)y} \mathbf{e}_x. \tag{6}$$

Hereby, infinitely long (y) magnets were assumed. j_0 and M_0 denote the averaged current density applied (σE_0) and the magnetization of the magnet, respectively. The spacing parameter a determines the "penetration depth" of the Lorentz force; larger values of a lead to Lorentz forces acting deeper inside the fluid. Fig. 3 illustrates the modulus of the spatial force distribution $\mathbf{f}_L$ around the foil at a penetration depth of $a/c = 0.1265$.

2.3. Governing equations

Based on chord length c of the hydrofoil and freestream velocity U_0, the governing equations in dimensionless form read for the 2-D case

$$\frac{\partial \mathbf{u}}{\partial t} + (\mathbf{u}\nabla)\mathbf{u} = -\nabla p + \frac{1}{Re}\Delta \mathbf{u} + N g(y^*) \mathbf{e}_t^*, \tag{7}$$

$$\nabla \cdot \mathbf{u} = 0, \qquad g(y^*) = \mathrm{e}^{-\pi(c/a)y^*}. \tag{8}$$

Hereby, y^* measures the local wall-normal distance, and $\mathbf{e}_t^*$ denotes the corresponding tangential direction vector along the foil. The amplitude function $g(y^*)$ is nonzero only above the active actuator range Δx at the suction side. End effects of the actuator in the oscillatory control regime where only a finite part Δx of the suction side is active, are approximately taken into account by a linear growth or decay of the force amplitude function $g(y^*)$ in a small transition range at the actuator ends while maintaining the total momentum input corresponding to Δx. The two dimensionless characteristic parameter of the problem are

$$Re = \frac{U_0 c}{\nu}, \qquad N = \frac{\pi}{4} \frac{j_0 B_0 c}{\rho U_0^2} \tag{9}$$

whereby besides the usual Reynolds number Re the interaction parameter N describes the ratio of electromagnetic to inertial forces. Here, ν denotes the kinematic viscosity of the fluid, and $M_0 = 2B_0$ is used assuming infinitely long magnets.[2]

In analogy to conventional control by blowing, a momentum coefficient may be introduced as

$$C_\mu = \frac{a j_0 B_0}{2\rho U_0^2} \cdot \frac{\Delta x}{c} \tag{10}$$

[2] For magnets of finite length, this factor is larger than two. In [18] it was assumed $M_0 = 8B_0/\pi$, yielding $N = j_0 B_0 c/(\rho U_0^2)$.

Table 1
Vector components of the integral in Eq. (15) (term in square brackets) versus penetration depth a/c

a/c	x-component	y-component
0.12650	0.042243	0.0015818
0.06325	0.020627	0.0003953
0.03163	0.010190	0.0000981

which describes the ratio of the total momentum added by the Lorentz force to the dynamic pressure. Hereby, Δx denotes the active part of the chord length where the actuator is active. In case of actuation over the whole chord length, as in the steady control regime below, from (9) it follows

$$C_\mu = \frac{2a}{\pi c} N. \tag{11}$$

In case of time-periodic forcing, by introducing a nondimensional frequency f based on chord length c and freestream velocity U_0, the Lorentz force amplitude function reads

$$g(y^*, t) = \mathrm{e}^{-\pi (c/a) y^*} \cos(2\pi f t), \qquad f = \frac{\tilde{f} \cdot c}{U_0}. \tag{12}$$

The corresponding momentum coefficient, based on the root-mean-square value of the force amplitude, is defined as

$$c'_\mu = \frac{\sqrt{2}}{2} N \frac{2a}{\pi c} \frac{\Delta x}{c}. \tag{13}$$

Forces acting on the hydrofoil are due to friction and pressure but additionally due to action of the Lorentz force. Based on dynamic pressure and chord length, the dimensionless total drag and lift coefficients used in the following are defined as

$$C_D = \frac{F_x}{(\rho/2) U_0^2 c}, \qquad C_L = \frac{F_y}{(\rho/2) U_0^2 c}, \tag{14}$$

where F_x and F_y denote the total force component per spanwise length unit in streamwise and normal direction, respectively. The part of the lift coefficient due to the momentum input of the Lorentz force will be denoted as C_M and follows from integration over the area above the active part of the actuator:

$$C_M = \frac{2N}{c^2} \left[\iint \mathrm{d}A \, \mathrm{e}^{-\pi (c/a) y^*} \mathbf{e}_t^* \right] \cdot \mathbf{e}_y. \tag{15}$$

Table 1 lists the vector components of the integral (in square brackets) for different values of the penetration depth a/c in case of actuation over the whole chord length at zero angle of attack. The x-component is roughly linearly depending on a/c, although for the largest value of a/c shown here, about 5% deviation occur due to the curvature of the characteristic polynom (1) of the foil. The y-component is much smaller and scales approximately quadratic for larger a/c.

3. Numerical method

A spectral element method is applied which advantageously combines the geometric flexibility of finite element methods with the high accuracy of global spectral methods. Hereby, spatial discretization inside the quadraliteral elements in the x–y plane is based on orthogonal Legendre polynom expansions of order $N_L \times N_L$. Extension to three-dimensional simulations with Fourier expansion in spanwise direction is already available for future work but is not used for the 2D simulations presented here. Time integration is based on a stiffly-stable scheme of up to third order [27], treating viscous terms implicitly and the nonlinear terms and the Lorentz force explicitly. The resulting Helmholtz equations can then be solved by direct or iterative conjugated gradient methods. Further details of the method which has already been successfully applied to EMHD problems [9–11] can be found in [28,29].

The computational domain with respect to width and position of the hydrofoil was chosen to resemble the test section geometry of an existing experimental facility and should allow later for comparison with experimental results.

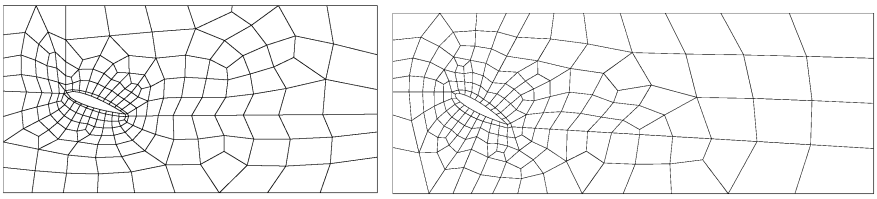

Fig. 4. Typical grids used in the computations. Left: 206 spectral elements; angle of attack $\alpha = 20°$. Right: 192 spectral elements; angle of attack $\alpha = 30°$.

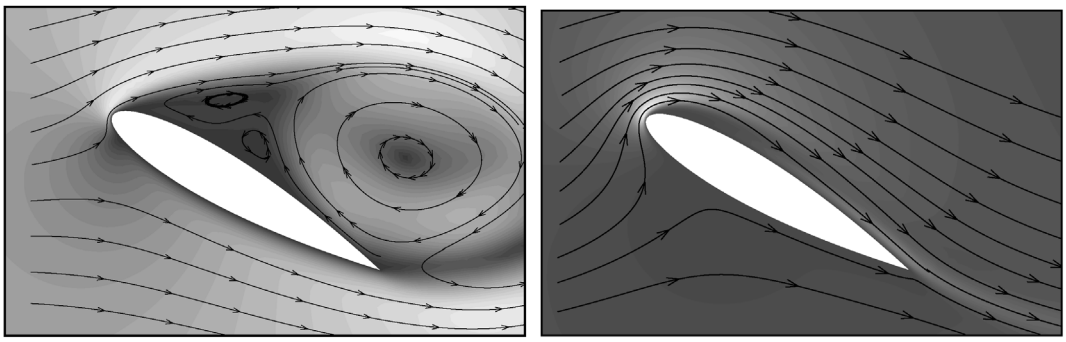

Fig. 5. Snapshots of the flow around a PTL-4 hydrofoil at $\alpha = 30°$, $Re = 500$. Shown are streamtraces and grey contours of u_x. Left side: without control ($N = 0$), right side: $N = 40$, $a/c = 0.1265$.

Grid generation for hydrofoils at different angles of attack in the rectangular domain was done by using the pre-processing capabilities of FIDAP 8.6.2 [30]. Typical grids as shown in Fig. 4 consist of about 200 spectral elements generated in such a way in order to ensure sufficient resolution at boundary and shear-layer regions in the near wake while trying to avoid computational overhead in low-shear regions. The grid at $\alpha = 30°$ covers a rectangular domain of $-1 \leqslant x \leqslant 7$ and $-1.5 \leqslant y \leqslant 1.5$. The center of gravity of the hydrofoil is located at ($x = 0.3$, $y = 0$).

The boundary conditions applied in the simulations are no-slip ($u = 0$, $v = 0$) at the hydrofoil and freestream ($u = 1$, $v = 0$) at inlet, top and bottom of the computational domain. At the outlet, outflow conditions of $(\mathbf{n} \cdot \nabla)\mathbf{u} = 0$ and $p = 0$ are applied where $\mathbf{n}$ denotes the boundary-normal direction vector. At all other boundaries, a high order pressure condition of Neumann type is used to minimize divergence errors induced by the splitting scheme [27]. Freestream boundary conditions at top and bottom of the domain were chosen to minimize resolution efforts.

To validate the accuracy of the numerical method, resolution studies at fixed grids by varying the inner element resolution $N_L \times N_L$ have been performed. For Reynolds numbers up to $Re = 600$ under investigation here, the final choice of $N_L = 9$ ensures lift and drag accuracy of about $\pm 1\%$ and is also in good agreement with resolutions used in bluff body flow simulations at comparable Reynolds numbers by a similar numerical method [11].

4. Results

4.1. Stationary forces

The following selected results summarize the capability of stationary Lorentz forces to delay or even to suppress separation. Hereby, the actuator is active on the entire suction side of the hydrofoil.

Fig. 5 shows snapshots of the uncontrolled flow around the hydrofoil at an angle of attack of 30° and the controlled flow under action of a Lorentz force of amplitude $N = 40$ and a penetration depth of $a/c = 0.1265$ at a Reynolds number of $Re = 500$. Clearly it is shown that the flow without control experiences separation, which can be completely suppressed when applying the Lorentz force. Furthermore, at this large value of the interaction parameter N, which corresponds to a momentum coefficient of about $C_\mu = 1.61$, the flow around the hydrofoil is almost steady, and a jet on the suction side can already be detected.

For larger values of the Reynolds number, with respect to practical applications in the turbulent range, complete suppression of separation might not be feasible as the necessary Lorentz force grows considerably [13]. However,

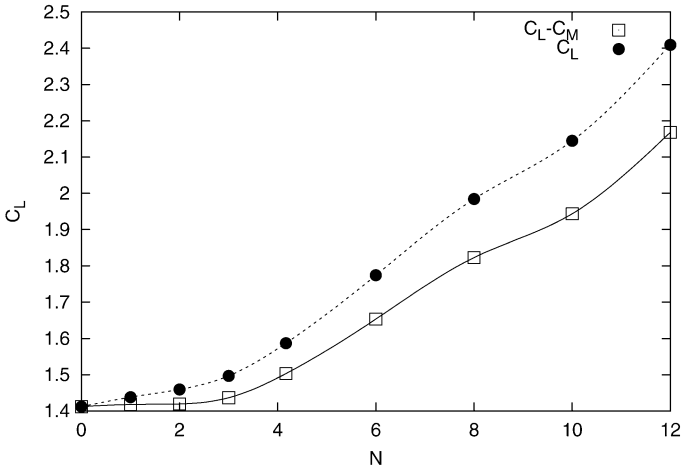

Fig. 6. Lift coefficient C_L as a function of the interaction parameter N. C_L–C_M denotes the part of C_L when the momentum input due to the Lorentz force C_M is not taken into account. $Re = 600$, $\alpha = 30°$, $a/c = 0.06325$.

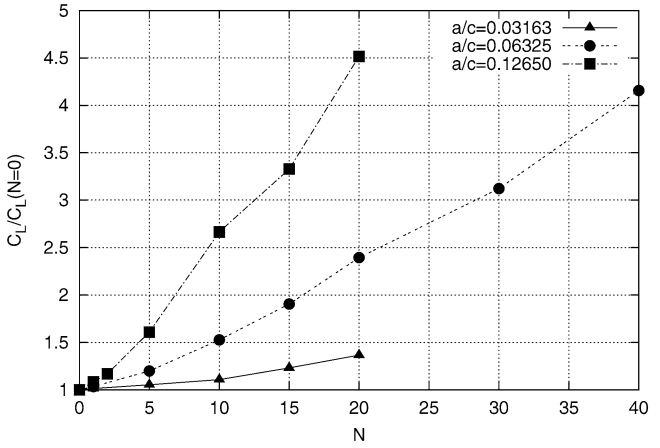

Fig. 7. Variation of the penetration depth a/c at $Re = 500$, $\alpha = 30°$.

already separation delay, in line with a downstream shift of the time-averaged separation point, might lead to considerable gains in the lift coefficient.

Fig. 6 shows the behavior of the time-averaged lift coefficient as a function of the interaction parameter at $Re = 600$, $\alpha = 30°$. Hereby, in the force balance, the momentum input due to the Lorentz force C_M grows only linearly with N whereas the total lift coefficient C_L seems to grow stronger than linearly. For small values of N, a quadratic dependence due to the separation delay is expected, until the flow is completely attached. However, in our numerical investigation, this might be disturbed by the finite channel width which influences the pressure field.

The variation of the penetration depth a/c offers a possibility for reducing the energy effort needed to achieve some fixed lift gain. However, doubling a at constant N requires a double energy input, as the electric resistance R is proportional to a. The energy input is furthermore proportional to $\sim N^2$ as $P_{\mathrm{el}} = R \cdot j_0^2 \cdot A$ where A denotes the electrode area. Fig. 7 shows the dependence of the lift coefficient gain $C_L(N)/C_L(N = 0)$ versus interaction parameter N for different values of the penetration depth a/c. In spite of the increased energy effort needed in case of the largest value of a/c, a net gain of efficiency in terms of lift gain per energy effort can be found. In general, for other flow configurations, at other values of the Reynolds number, where the ratio between boundary layer thickness and penetration length changes, the result might differ. However, it seems to be advantageous to choose a/c not smaller than a characteristic boundary layer thickness of the flow. For the above case, it holds $\delta_{\mathrm{lam}} \sim 1/\sqrt{Re} \approx 0.044$ and $a/c \approx 0.063$.

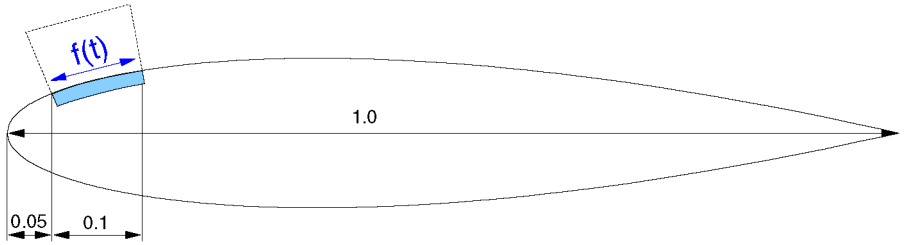

Fig. 8. PTL-4 profile with marked actuator range in the front part: $0.05 \leqslant x/c \leqslant 0.15$.

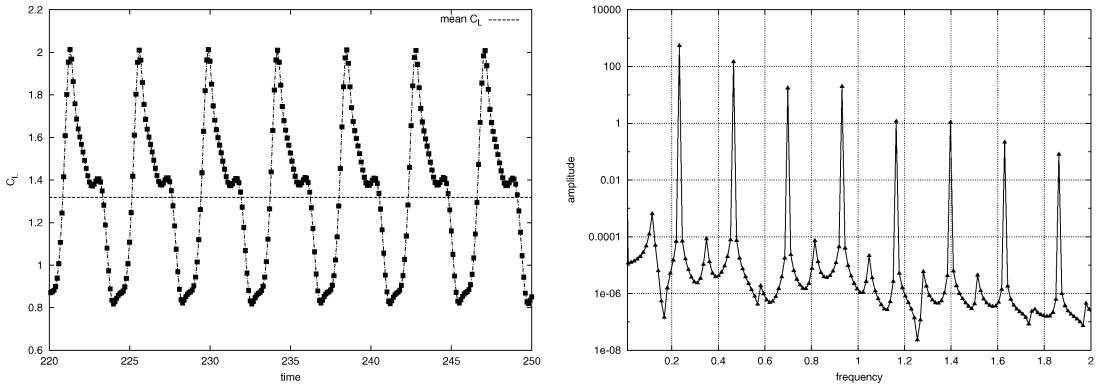

Fig. 9. Left: lift coefficient C_L and its temporal mean value at $Re = 500$, $\alpha = 30°$, without control. Right: corresponding power spectrum of C_L.

4.2. Oscillatory forcing

Following the shear-layer phenomenology, oscillatory actuation should be applied at the front part of the hydrofoil. Of course, the optimum position of the actuator depends on flow details as, e.g., the position of the separation point. In the following, we present results at a Reynolds number of $Re = 500$ and an angle of attack of $\alpha = 30°$ where the uncontrolled flow is already separated (see Fig. 5). The active actuator range was chosen as $0.05 \leqslant x/c \leqslant 0.15$ (see Fig. 8), and the penetration depth of the Lorentz force is $a/c = 0.1265$.

Fig. 9 shows on the left side the transient behavior of the lift coefficient without control. The time signal looks periodic with a mean lift coefficient of $C_L^0 = 1.318$. Because vortex shedding is not symmetric from suction and pressure side of the inclined foil, sharp maxima at $C_L^0 + 0.68$ and broader minima at $C_L^0 - 0.51$ occur, yielding a total amplitude of lift oscillations of about $\Delta C_L^0 \approx 1.19$. The dominant frequency of the lift signal is about $f_0 \approx 0.233$ which corresponds to the largest lift oscillations caused by the periodic shedding of vortices. On the right side, the corresponding power spectrum of the lift coefficient is shown which exhibits a distinct maximum at exactly this frequency and further peaks of decaying height at its harmonics $2f_0 \approx 0.466$, $3f_0 \approx 0.699$ etc.

In the low Reynolds number range investigated here, similar to rotary or oscillatory control of the cylinder flow and the lock-in behavior found there [20,21,31], a large control receptivity should be expected at excitation frequencies close to the main shedding frequency f_0 of the uncontrolled flow and the first harmonics of it. At higher harmonics, receptivity typically decreases because of inertia.

At a Reynolds number of $Re = 500$, with respect to the temporal behavior of the lift coefficient, a large variety of flow phenomena exists, including periodic, multiple-frequency, intermittent and acyclic behavior. Fig. 10 shows the temporal behavior of the lift coefficient C_L without control and for selected values of the excitation frequency f at different values of the interaction parameter N, superimposed with the corresponding control amplitude $g(0, t)$ from Eq. (12). Hereby, the scaling of the lift axis is kept fixed except for the case $N = 20$, $f = 0.53$ where large fluctuations occur. At all parameter values shown here, the time signal is periodic, which is, of course, not the case in general at this Reynolds number. The frequencies were selected according to the discussion of the mean lift as will be seen below.

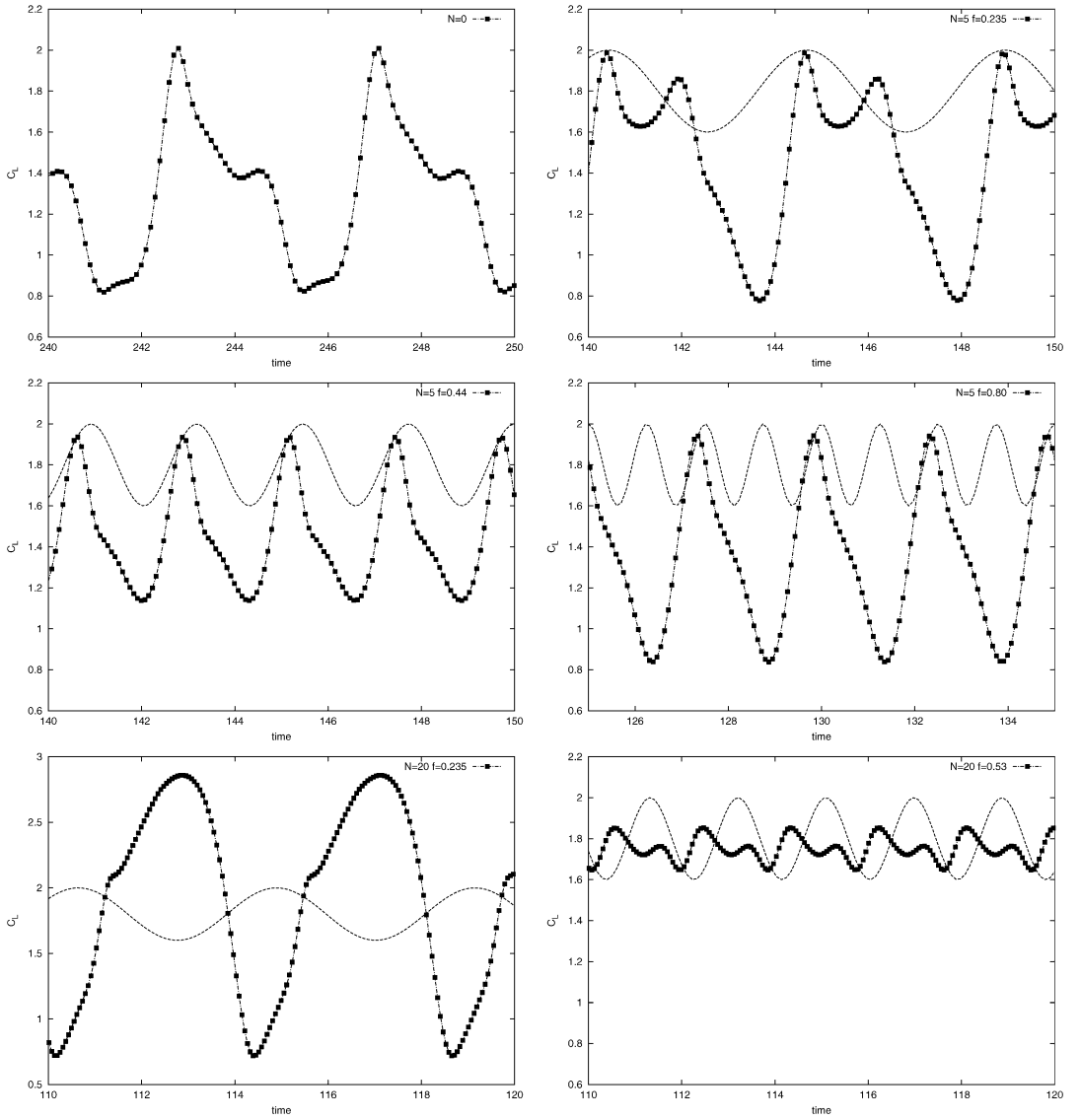

Fig. 10. Time signal of the lift coefficient C_L without control and at various values of the interaction parameter N and the control frequency f, superimposed with the corresponding excitation signal of fixed artificial amplitude. Please note a modified C_L-scaling at $N = 20,\ f = 0.235$.

Fig. 11 shows on top the streamtraces of the time-averaged flow in case without control. During one period, vortices of different size are shed, leading to the temporal behavior of the lift shown in Fig. 10. Minimum lift is related to the periodic build-up of a large separation bubble, and maximum lift is achieved shortly after its release from the foil surface.

Now, introducing a relatively weak control amplitude of $N = 5$ at a frequency of $f = 0.235$ (which is close to the dominant shedding frequency in the no-control case) leads to a slightly modified shedding process as in Fig. 10 almost a double peak of the lift maxima appears, which in turn (see below) leads to a larger mean value of the lift. Hereby, the maxima of the control amplitude are locked-in with the lift maximum as the downstream momentum of the control minimizes separation. On the other hand, upstream forcing certainly forces separation, i.e. in general, provided control is strong enough, the lift signal should follow the sinusoidal shape of the excitation, leading also to a smaller size of the largest separation bubble as compared to the uncontrolled flow.

At an excitation frequency of $f = 0.44$, which is roughly twice the natural frequency f_0 of the uncontrolled flow, the lift signal now synchronously follows the external excitation. Furthermore, the lift oscillations now have

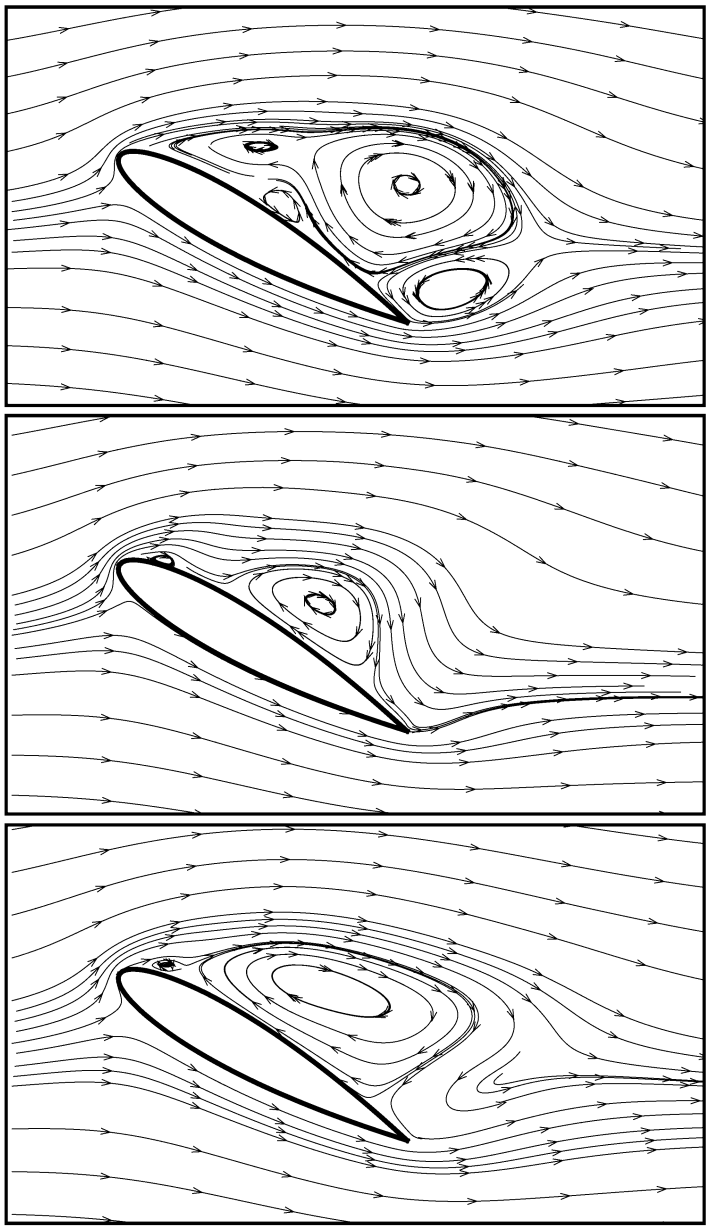

Fig. 11. Streamtraces of the time-averaged flow at $Re = 500$, $\alpha = 30^\circ$, $N = 0$ (top), $N = 20$, $a/c = 0.1265$, $f = 0.235$ (middle) and $f = 0.53$ (bottom).

considerably decreased as compared to the two upper cases. Lift is almost inphase with the excitation, lift maxima are achieved slightly before excitation reaches the maximum.

At an excitation frequency of $f = 0.80$, the lift signal looks similar to the case of $f = 0.44$ although the lift oscillations again are as big as in the uncontrolled case. External forcing here is not strong enough to synchronize the vortex shedding with the control frequency completely – both maxima and minima of the lift curve are locked with maxima of the excitation force which varies twice as fast as the lift does.

Despite the clear influence of oscillatory control at amplitude $N = 5$ on vortex shedding and lift, changes in the streamtraces of the time-averaged flow as shown in Fig. 11 for the uncontrolled flow are rather weak and therefore not shown. However, increasing the control amplitude to an interaction parameter of $N = 20$ gives a strong effect, as can be seen from the two lower pictures in Fig. 11, shown for $f = 0.235$ and $f = 0.53$. The temporal behavior of the

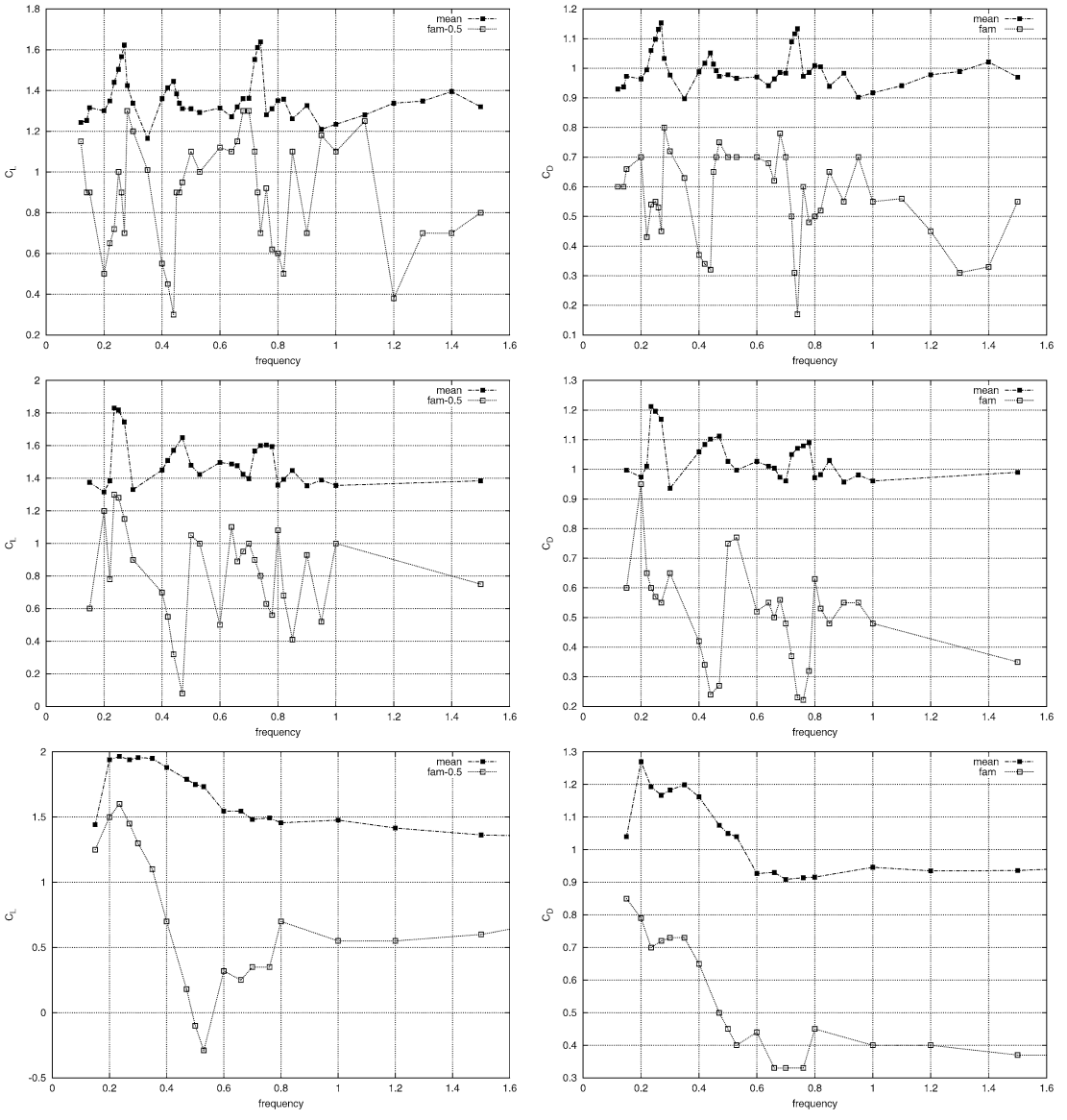

Fig. 12. Lift and drag coefficient C_L and C_D (left to right) at control amplitudes $N = 5$; 10; 20 (top to bottom) versus excitation frequency f. Hereby, "mean" and "fam" denote the mean value and the fluctuation amplitude, respectively.

lift coefficient C_L at these two selected control frequencies is shown in Fig. 10. At $f = 0.235$, there are very large lift oscillations following the external excitation which is close to the natural shedding frequency f_0. However, phase shift between lift and excitation amplitude is 180°. The corresponding streamtrace figure of the time-averaged flow (Fig. 11, middle) already indicates that lift must have been increased considerably as the mean separation bubble is much smaller now than in the uncontrolled case.

At a larger excitation frequency of $f = 0.53$ lift oscillations are minimum but follow the external excitation frequency with only a small phase shift. The time-averaged flow picture again looks closer to the uncontrolled case.

Fig. 12 summarizes the behavior of the lift and drag coefficient versus excitation frequency at three different values of the forcing amplitude N. In each subfigure, the mean and its fluctuation amplitude (for the lift: $\Delta C_L = C_L^{\max} - C_L^{\min}$), sometimes shifted for convenience, is shown. For weak control amplitudes of $N = 5$, two clear maxima of both the mean lift and the mean drag coefficient exist at $f \approx 0.27$ and $f \approx 0.74$. At $f \approx 0.44$ a smaller maximum

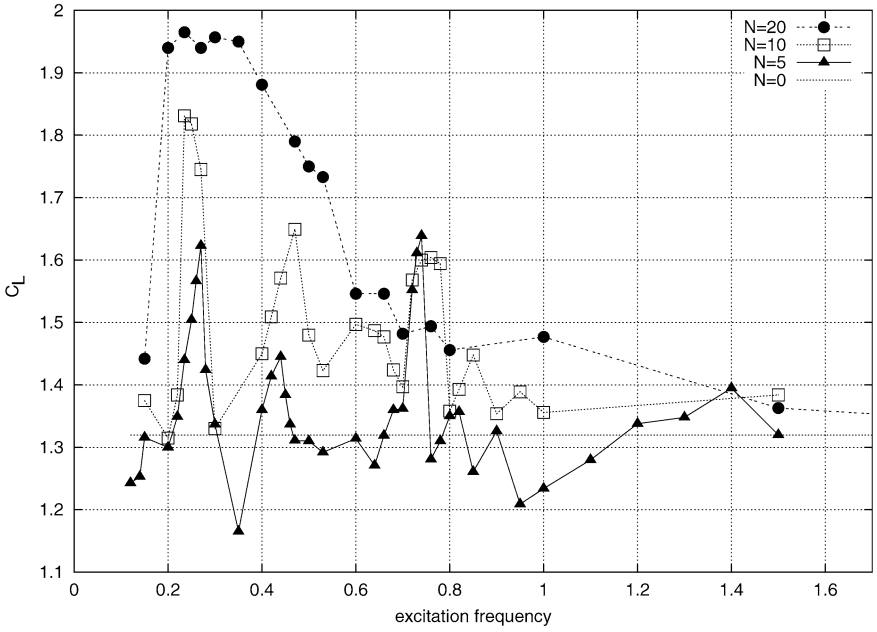

Fig. 13. Mean lift coefficient versus excitation frequency at different amplitudes N; $a/c = 0.1265$.

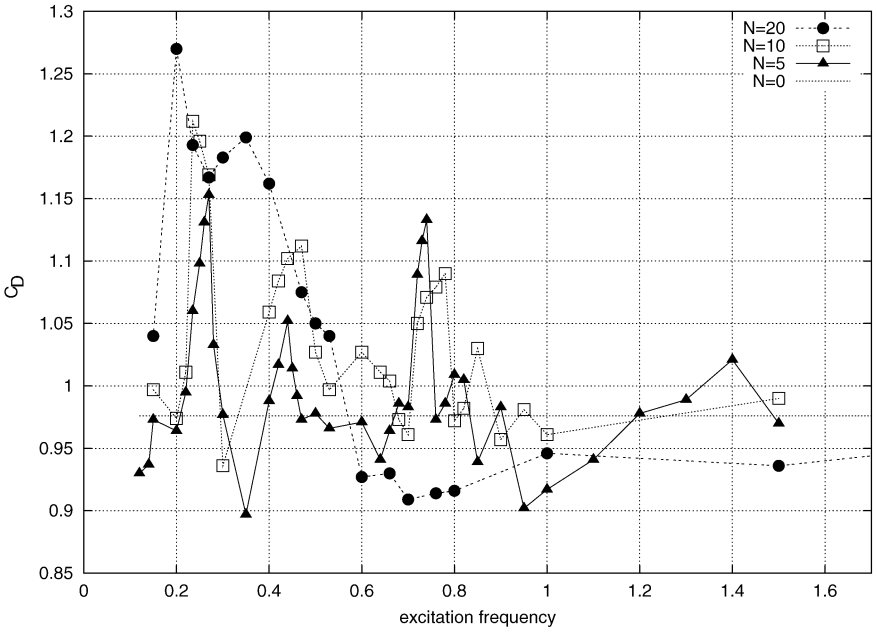

Fig. 14. Mean drag coefficient versus excitation frequency at different amplitudes N; $a/c = 0.1265$.

can be found. These maxima are close to frequencies where the lift fluctuations are maximum except the smaller peak at $f \approx 0.44$, although no clear picture exists at this weak control amplitude.

Stronger control of $N = 10$ gives maximum lift and drag at $f \approx 0.235$ and smaller maxima at $f \approx 0.47$ and at $f \approx 0.76$. The lift fluctuations are maximum at the natural shedding frequency f_0 and are minimum at the first harmonic of it at $f \approx 0.47$.

Increasing the control further to $N = 20$, a broader maximum around the natural shedding frequency of $f = 0.235$ appears which now contains inside the two maxima of the lift curve at lower control amplitudes. The third maximum

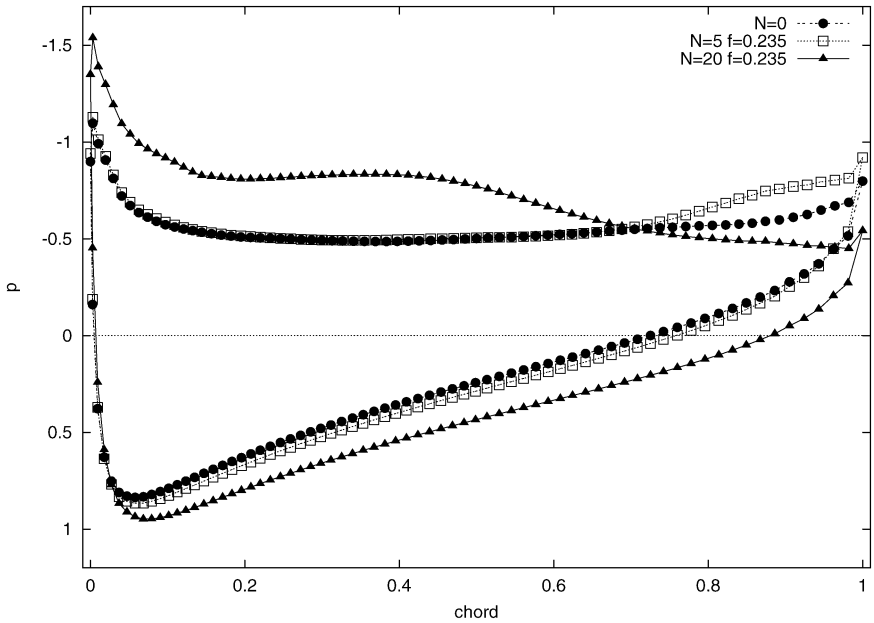

Fig. 15. Surface pressure at suction and pressure side of the foil versus chord coordinate at excitation frequency $f = 0.235$, $Re = 500$, $\alpha = 30°$ for different control amplitudes N. Please note a reversed pressure axis.

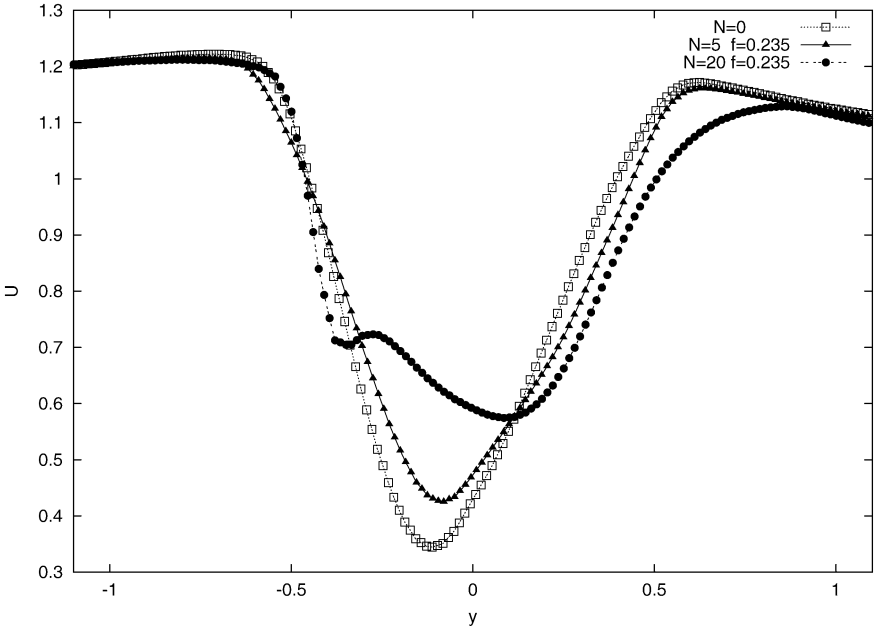

Fig. 16. Time-averaged wake profiles of the streamwise velocity component at $x = 1.5$ for $Re = 500$, $\alpha = 30°$.

has disappeared as with increasing force amplitude, increased inertia of the flow make higher frequency oscillations less effective. At the natural shedding frequency, lift fluctuations are maximum, and minimum lift fluctuations occur at $f \approx 0.53$.

Figs. 13 and 14 summarize the behavior of the mean lift and drag coefficient versus actuation frequency f at different values of the interaction parameter N. For a weak control amplitude of $N = 5$, there exist distinct maxima for both lift and drag coefficient where a weak control influence is sufficient to advantageously modify the process of vortex shedding. Stronger control in general leads to larger gains in lift but also to larger drag penalties. With growing

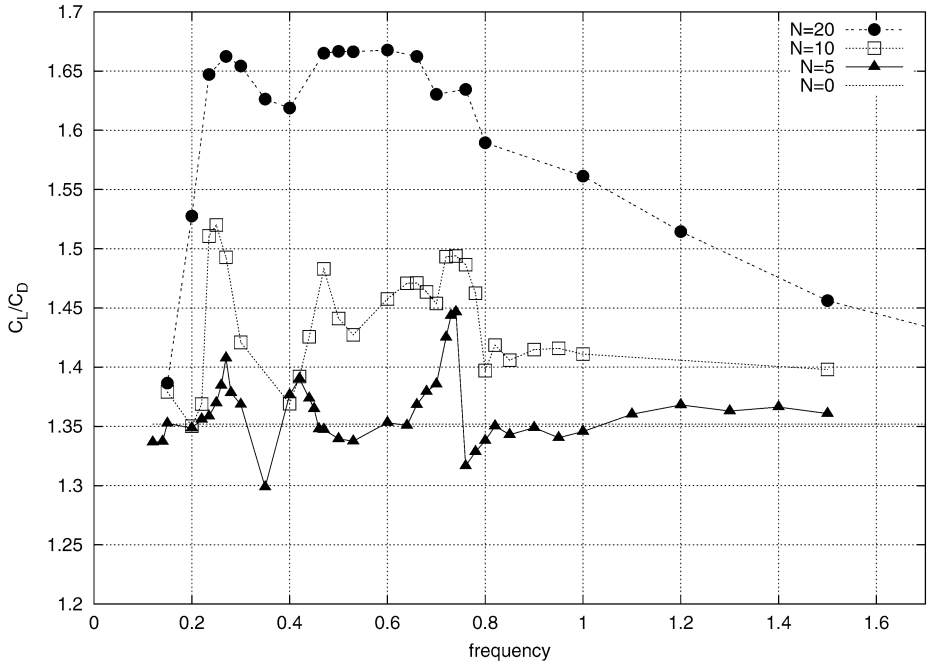

Fig. 17. Hydrofoil efficiency C_L/C_D versus excitation frequency at different amplitudes N; $a/c = 0.1265$, $\alpha = 30°$.

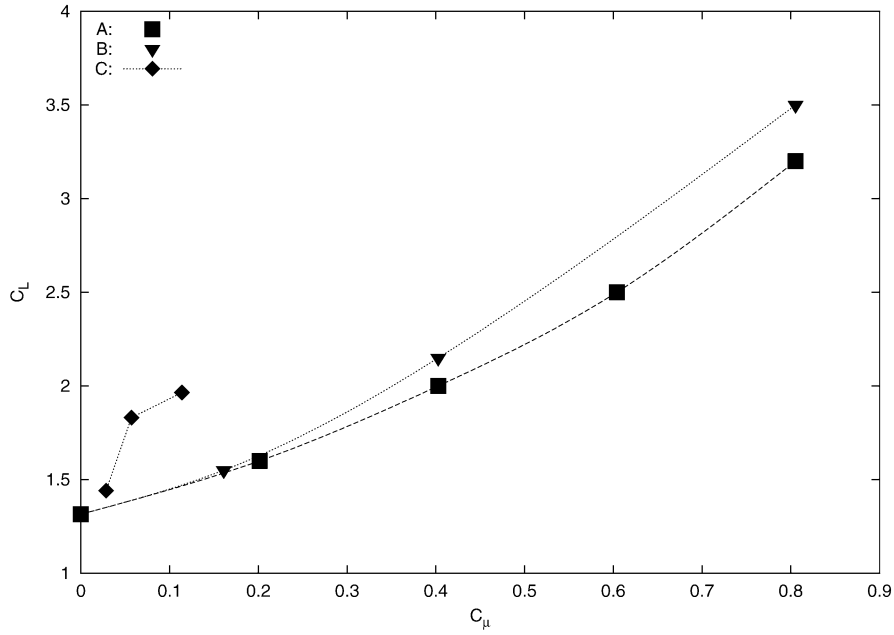

Fig. 18. Comparison of the lift coefficient versus momentum coefficient, obtained by steady (A: $a/c = 0.06325$, B: $a/c = 0.1265$) and oscillatory forcing (C: $a/c = 0.1265$, $f = 0.235$), at $Re = 500$, $\alpha = 30°$.

control amplitude, largest lift and, at the same time, largest drag, is observed more and more in a broad band of frequencies around the natural shedding frequency, and the importance of higher excitation frequencies decays because of inertia. The lift gain obtained in the broad frequency band mentioned above corresponds to only a modification of the natural vortex shedding by a strong external excitation. This phenomenon is similar to the lock-in behavior found in the oscillatory cylinder control [21,24,31].

Fig. 15 shows the behavior of the pressure of the time-averaged flow at the foil surface versus chord coordinate at excitation frequency $f = 0.235$, $Re = 500$, $\alpha = 30°$ for different values of the control amplitude N. For $N = 5$, there is only a weak modification as compared to $N = 0$, whereas for $N = 20$ a clear increase of p at the pressure side and a modified behavior at the suction side according to the smaller separation bubble shown in Fig. 11 is found. Although here rear pressure is larger, in the front and middle part pressure is considerably decreased with a larger negative peak at the front.

Fig. 16 shows time-averaged profiles of the streamwise velocity component in the wake at $x = 1.5$ at excitation frequency $f = 0.235$ for different control amplitudes. The broadening of the velocity defect is in line with the increase of drag found at this excitation frequency when the control amplitude is increasing. Although lift enhancement is usually coupled to drag penalty, as can be seen from Fig. 17, the efficiency of the hydrofoil defined as ratio of C_L/C_D enhances in the frequency band around the natural shedding frequency f_0.

4.3. Comparison with steady control

Fig. 18 compares the lift enhancement obtained at the optimum frequency of $f = 0.235$ with results obtained by steady control at different values of the penetration depth a/c at a Reynolds number of $Re = 500$ and an angle of attack of $\alpha = 30°$. As mentioned already above, the larger value of the penetration depth a/c is preferable in case of steady control. But, at small values of the momentum coefficient, oscillatory control is clearly more effective than steady control. At these values of the momentum coefficient, steady flow control only achieves a small amount of separation delay, whereas oscillatory control is already able to reorganize vortex shedding because of the large receptivity of the uncontrolled flow to the optimum excitation frequency. For larger values of the momentum coefficient, steady forcing might become more effective since oscillatory forcing can not completely suppress separation.

5. Discussion

In the post-stall flow regime around an inclined hydrofoil, steady control is capable of suppressing separation completely if the Lorentz force amplitude is large enough. On the other hand, oscillatory control applied to the front part of the suction side has always to struggle with the natural process of vortex shedding, thereby only modifying it. However, if proper excitation frequencies are chosen, periodic control can be more effective than steady control in terms of the momentum coefficient.

Oscillatory control leads to interesting flow phenomena which deserve further investigation as the present work was focused on the influence on the behavior of lift and drag. Similarities to the lock-in phenomena in the oscillatory cylinder control [21,24,31] were found. Weak control can lead to lift enhancement at frequencies around the natural shedding frequency and its first harmonics, although a strong sensibility to small frequency changes exists. With increasing control amplitude, control at larger frequencies becomes less effective, and a frequency band around the natural shedding frequency gives maximum lift. In both cases, steady and oscillatory control, increase of lift is always connected with increased drag, although airfoil efficiency is enhanced. These results are similar to what is found at much larger Reynolds numbers in the transitional and turbulent flow regime [2,14]. However, optimum control frequencies found there are typically about one and therefore different from the smaller optimum frequencies of $f \sim 0.2$ found here. As a clear relation of optimum excitation to vortex shedding can be stated in our case, the wake influence is strong and seems to dominate, whereas at larger Reynolds numbers arguments from the shear layer are used [2]. However, Wu et al. [3] and recently also Darabi and Wygnanski [32] stress the relation of periodic excitation and vortex shedding at large Reynolds numbers as always a complex coupling of shear layer instability, separation bubble and wake characteristics exists. If instead chord-length a typical stream-normal length-scale (foil cross-stream length or wake width) is used to non-dimensionalize frequency, it becomes clear that these optimum frequencies are also close to the natural frequency of vortex shedding.

Acknowledgements

We are grateful to G.E. Karniadakis and his group at Brown University for introducing us into the code PRISM. The computations were performed at the computing center of Forschungszentrum Rossendorf. We further acknowledge

fruitful discussions with T. Weier in preparation of this work. Financial support from DFG in frame of Sonderforschungsbereich 609 is gratefully acknowledged.

References

[1] M. Gad-el-Hak, Flow Control, Cambridge University Press, 2000.
[2] D. Greenblatt, I.J. Wygnanski, The control of flow separation by periodic excitation, Prog. Aero. Sci. 36 (2000) 487–545.
[3] J.-Z. Wu, X.-Y. Lu, A.G. Denny, M. Fan, J.-M. Wu, Post-stall flow control on an airfoil by local unsteady forcing, J. Fluid Mech. 371 (1998) 21–58.
[4] E.L. Resler, W.R. Sears, The prospects for magneto-aerodynamics, J. Aero. Sci. 25 (1958) 235–245.
[5] A. Gailitis, O. Lielausis, On the possibility to reduce the hydrodynamical resistance of a plate in an electrolyte, Appl. Magnetohydrodyn. Rep. Riga Inst. Phys. 12 (1961) 143–146 (in Russian).
[6] C. Henoch, J. Stace, Experimental investigation of a salt water turbulent boundary layer modified by an applied streamwise magnetohydrodynamic body force, Phys. Fluids 7 (1995) 1371–1383.
[7] C. Crawford, G.E. Karniadakis, Reynolds stress analysis of EMHD-controlled wall turbulence. Part I. Streamwise forcing, Phys. Fluids 9 (1997) 788–806.
[8] T.W. Berger, J. Kim, C. Lee, L. Lim, Turbulent boundary layer control utilizing the Lorentz force, Phys. Fluids 12 (3) (2000) 631–649.
[9] Y. Du, G.E. Karniadakis, Suppressing wall turbulence by means of a transverse travelling wave, Science 288 (2000) 1230–1234.
[10] Y. Du, V. Symeonidis, G.E. Karniadakis, Drag reduction in wall-bounded turbulence via a transverse travelling wave, J. Fluid Mech. 457 (2002) 1–34.
[11] O. Posdziech, R. Grundmann, Electromagnetic control of seawater flow around circular cylinders, Eur. J. Mech. B Fluids 20 (2001) 255–274.
[12] S.-J. Kim, C.M. Lee, Investigation of the flow around a circular cylinder under the influence of an electromagnetic force, Exp. Fluids 28 (2000) 252–260.
[13] T. Weier, G. Gerbeth, G. Mutschke, O. Lielausis, G. Lammers, Control of flow separation using electromagnetic forces, Flow, Turbulence and Combustion 71 (2003) 5–17.
[14] T. Weier, G. Gerbeth, Control of separated flows by time-periodic Lorentz forces, Eur. J. Mech. B Fluids 23 (6) (2004) 835–849.
[15] P.B.S. Lissaman, Low-Reynolds-number airfoils, Annu. Rev. Fluid Mech. 15 (1983) 223–239.
[16] D. Greenblatt, I. Wygnanski, Use of periodic excitation to enhance airfoil performance at low Reynolds numbers, J. Aircraft 38 (2001) 190–192.
[17] Y. Hoarau, D. Faghani, M. Braza, R. Perrin, D. Anne-Archard, D. Ruiz, DNS of the 3-D transition to turbulence in the incompressible flow around a wing, Flow, Turbulence and Combustion 71 (2003) 119–132.
[18] T. Weier, G. Gerbeth, G. Mutschke, E. Platacis, O. Lielausis, Experiments on cylinder wake stabilization of an electrolyte solution by means of electromagnetic forces localized on the cylinder surface, Exp. Therm. Fluid Sci. 16 (1998) 84–91.
[19] P. Poncet, Vanishing of mode B in the wake behind a rotationally oscillating circular cylinder, Phys. Fluids 14 (6) (2002) 2021–2023.
[20] G.E. Karniadakis, G.S. Triantafyllou, Frequency selection and asymptotic states in laminar wakes, J. Fluid Mech. 199 (1989) 441–469.
[21] S. Choi, H. Choi, S. Kang, Characteristics of flow over a rotationally oscillating cylinder at low Reynolds number, Phys. Fluids 14 (8) (2002) 2767–2777.
[22] T. Weier, G. Gerbeth, G. Mutschke, U. Fey, O. Posdziech, O. Lielausis, E. Platacis, Some results on electromagnetic control of flow around bodies, in: Proc. Int. Symp. “Seawater Drag Reduction”, Newport, RI, July 22–24, 1998.
[23] S. Taneda, Visual observations of the flow past a circular cylinder performing a rotary oscillation, J. Phys. Soc. Jpn. 45 (1978) 3114–3116.
[24] P.T. Tokumaru, P.E. Dimotakis, Rotary oscillation control of a cylinder wake, J. Fluid Mech. 224 (1991) 77–90.
[25] V.I. Shatrov, V.I. Yakovlev, Optimization of the internal source in the problem of MHD flow around a sphere, J. Appl. Mech. Techn. Phys. 33 (1992) 334–341.
[26] V. Avilov, Electric and magnetic fields for the Riga plate, Technical Report, FZR, Rossendorf, July 1998.
[27] G.E. Karniadakis, M. Israeli, S.A. Orszag, High-order splitting methods for the incompressible Navier–Stokes equations, J. Comp. Phys. 97 (1991) 415–443.
[28] R.D. Henderson, G.E. Karniadakis, Unstructured spectral element methods for simulation of turbulent flows, J. Comp. Phys. 122 (1995) 191–217.
[29] G.E. Karniadakis, S.J. Sherwin, Spectral/hp Element Methods for CFD, Oxford University Press, 1999.
[30] FIDAP 8.0; Fluent Inc., 2002.
[31] S. Mittal, Control of flow past bluff bodies using rotating control cylinders, J. Fluids Struct. 15 (2001) 291–326.
[32] A. Darabi, I. Wygnanski, Active management of naturally separated flow over a solid surface. Part 1. The forced reattachment process, J. Fluid Mech. 510 (2004) 105–129.